AIAA-90-0592

Similarity Models for Viscous Vortex Cores

Ernst W. Mayer
Kenneth G. Powell

Department of Aerospace Engineering
The University of Michigan
Ann Arbor, Michigan

28th Aerospace Sciences Meeting
January 8-11, 1990/Reno, Nevada

Similarity Models for Viscous Vortex Cores

Ernst W. Mayer*
Kenneth G. Powell †

The University of Michigan
Department of Aerospace Engineering

January 1990

Abstract

Results are presented for a new class of self–similar solutions to the steady, axisymmetric Navier–Stokes equations, modelling the flows in vortices whose viscous cores grow proportionally to an arbitrary power of the axial coordinate. Effects of Reynolds number, growth rate, free–stream Mach number and vortex strength are investigated. Results for incompressible vortices are compared to experimental results for leading-edge vortices and to the inviscid limiting case. It is shown that the core of an incompressible vortex should, in absence of an axial pressure gradient, grow with the one-half power of the axial coordinate. The total pressure level on the axis of the vortex is seen to be independent of Reynolds number and assumed growth rate, although the distribution of total pressure in the core is dependent on both. Large axial velocity surpluses are seen in the core as well as strong pressure gradients. Results for the viscous compressible vortex are compared to the inviscid potential and rotational model flows. Near–zero densities and pressures and very low temperatures are seen on the axis for reasonable freestream Mach numbers and vortex strengths. The presence of viscosity prevents the density from actually reaching zero, unlike with the inviscid models. Limiting velocity concepts are found to restrict the possible vortex strengths for a given freestream Mach number. Compressibility is shown to have a significant influence upon the distribution of vorticity in the core of the vortex.

Introduction

Vortex flows occur in nearly every area of continuum fluid mechanics – from the stirred fluid in a teacup to the flows in tornado funnels and hurricanes. An important instance of vortices in aerodynamics is the flow about a slender delta wing at angle of attack, in which the rolling up of the vortex sheets over the leading edges produces a vortex pair. These leading–edge vortices often have a roughly axisymmetric core region where viscous effects dominate the flow, and velocities and pressure gradients may be large.

Experimental studies of incompressible flows past delta wings have shown some remarkable features, including core velocities that are four to five times the free–stream values, accompanied by high gradients in the static and total pressures [1]. Experimental studies of compressible flows past delta wings have shown similar velocity and pressure gradients, accompanied by near–vacuum values of density on the core axis [2].

Analytical and numerical studies of incompressible leading–edge vortices have duplicated, at least qualitatively, many of these results. The incompressible models of Hall [3], Stewartson and Hall [4] and Powell and Murman [5] give axial velocity and static pressure values that agree fairly well with the experimental results of Earnshaw [1].

Theoretical studies of compressible vortices have given less satisfactory results. The compressible model of Brown [6] for an inviscid rotational flow shows that compressibility has a boundary-layer effect on the velocity field, but exhibits some odd behavior at higher Mach numbers. Mack [7]studied a viscous heat–conducting compressible vortex, but the flow field is a rather contrived one, with density becoming unbounded at the surface of a rotating cylinder in

*Doctoral Candidate, AIAA Member
†Assistant Professor, AIAA Member

the core which drives the flow. Hall [8] has given qualitative arguments concerning some of the expected features of compressible vortex cores, but there is at present no comprehensive theory in this area.

In recent years the availability of ever faster computers and improved algorithms has led many researchers to abandon any simplification of the governing equations and to perform directly two and three-dimensional calculations for geometries and flow conditions of current interest. Numerical solutions of the Euler and Navier-Stokes equations for flows past delta wings have obtained vortex structures [9, 10, 11] and pitot pressures that are consistent with those seen experimentally [12, 10, 13]. However, much may still be learned about the fundamental fluid mechanical processes at work in these problems without introducing the additional complexities of multidimensionality and flow boundaries. This is especially true for vortical flows, where variations in flow quantities may occur primarily in one spatial coordinate. This can lead to a tremendous simplification of the governing equations, making their solution straightforward and the results relatively easy to interpret, even making analytical solutions possible in some cases. This approach is the basis of this study. Under certain assumptions about the nature of the flow the governing equations reduce to a set of ordinary differential equations with appropriate boundary conditions, the solution of which is straightforward. This minimizes the number of parameters and allows the effects of each to be examined in detail. Much remains to be understood about such flows, and such analytical and simplified numerical methods can provide general insight into the physical processes occurring in them.

1 Methods for Incompressible Vortex Cores

1.1 Governing Equations

The governing equations are the equation of conservation of mass (continuity) and the Navier–Stokes equations of conservation of momentum, which for a steady, axisymmetric, incompressible flow may be written, in non-dimensional form, as:

$$\frac{1}{r}\frac{\partial}{\partial r}(ru) + \frac{\partial w}{\partial z} = 0 \tag{1a}$$

$$u\frac{\partial u}{\partial r} + w\frac{\partial u}{\partial z} - \frac{v^2}{r} = -\frac{\partial p}{\partial r} + \frac{1}{Re_L}\left[\frac{1}{r}\frac{\partial}{\partial r}\left(r\frac{\partial u}{\partial r}\right) + \frac{\partial^2 u}{\partial z^2} - \frac{u}{r^2}\right] \tag{1b}$$

$$u\frac{\partial v}{\partial r} + w\frac{\partial v}{\partial z} + \frac{uv}{r} = \frac{1}{Re_L}\left[\frac{1}{r}\frac{\partial}{\partial r}\left(r\frac{\partial v}{\partial r}\right) + \frac{\partial^2 v}{\partial z^2} - \frac{v}{r^2}\right] \tag{1c}$$

$$u\frac{\partial w}{\partial r} + w\frac{\partial w}{\partial z} = -\frac{\partial p}{\partial z} + \frac{1}{Re_L}\left[\frac{1}{r}\frac{\partial}{\partial r}\left(r\frac{\partial w}{\partial r}\right) + \frac{\partial^2 w}{\partial z^2}\right] . \tag{1d}$$

Here u, v and w are the radial, azimuthal and axial components of the velocity vector in cylindrical polar coordinates r, θ and z. The Reynolds number Re_L is based on a reference length L and the axial velocity at the edge of the region of interest, which is denoted by w_e. All velocities are nondimensionalized by w_e and the pressure is normalized by $\rho {w_e}^2$, where ρ is the mass density of the fluid.

The first of these equations expresses conservation of mass; the others represent conservation of radial, azimuthal and axial momentum, respectively. The most practical way to simplify these equations is to assume that flow quantities are self–similar relative to some set of coordinates related to the cylindrical coordinates through an appropriate coordinate transformation.

1.2 General Similarity Coordinates

Several similarity–based theoretical models for the incompressible leading–edge vortex have been advanced, differing mainly in their approach to the viscid–inviscid coupling which occurs in the core. Many have assumed a linear growth rate for the vortex, based on the fact that the shear layer rolling up from the leading edge of a delta wing grows in a roughly linear fashion with distance from its apex. However, it appears that even if the outer flow field grows in a conical fashion, the viscous core does not. To be able to treat a self–similar vortex core without assuming a specific growth rate in advance, the following general set of orthogonal coordinates is introduced:

$$\phi = \frac{r}{z^n} \quad , \quad \zeta = (nr^2 + z^2)^{1/2} . \tag{2}$$

Here, ϕ is a "radial" and ζ an "axial" coordinate. The azimuthal coordinate θ remains unchanged under the transformation. For various values of n, these coordinates represent families of mutually perpendicular curves in a plane θ = constant. For $n = 1$ these curves are rays and circles, for $n = 1/2$ they are parabolas and ellipses and for $n = 0$ the original coordinates are recovered, i.e. $\phi = r$ and $\zeta = z$.

If derivatives in the ζ–direction vanish, i.e. if it is assumed that the flow is self–similar, then the parameter n sets the rate of growth of the vortex with increasing z. If the radial extent of the viscous core is characterized by some location r_{edge}, then $n = 1/2$ and $n = 1$ correspond to parabolic ($r_{edge} \propto z^{1/2}$) and conical ($r_{edge} \propto z^1$) vortex growth, respectively. The $n = 0$ case represents a columnar vortex.

Most analyses based on similarity assume that the Reynolds number is high and the vortex is slender, i.e. that $\phi_{edge} \ll 1$. It is important to note that there are two distinctly different limits as the Reynolds number becomes large, leading to a different balances of terms in the governing equations. The first is the inviscid limit which assumes that as $Re \to \infty$, $\phi \to 0$ in such a fashion that $Re\phi^2 \to \infty$. In this limit the viscous terms become negligible, meaning that there is no longer a viscous core. The second, the viscous limit, assumes that as $Re \to \infty$, $\phi \to 0$ but the product $Re\phi^2$ is order of unity, implying that a viscous region is always present, but which becomes vanishingly small as $Re \to \infty$. These limits lead to different equations and boundary procedures, which will be described in detail in the next two sections.

1.3 The Inviscid Incompressible Leading–Edge Vortex

If the governing equations are transformed to the general similarity coordinates introduced in Section 1.2 and the inviscid limit taken as $Re \to \infty$ and $\phi \to 0$, the following set of ordinary differential equations is obtained, expressing conservation of mass and r, θ and z–momentum:

$$-\phi\left(nw - \frac{u}{\phi}\right)' + \frac{2u}{\phi} = 0 \tag{3a}$$

$$p' = \frac{v^2}{\phi} \tag{3b}$$

$$-\phi\left(nw - \frac{u}{\phi}\right)v' + \frac{uv}{\phi} = 0 \tag{3c}$$

$$-\phi\left(nw - \frac{u}{\phi}\right)w' + nv^2 = 0\,. \tag{3d}$$

The boundary conditions are taken to be

$$\phi = 0 : u = 0\,, \qquad \phi = \phi_e : \begin{cases} v = v_e \\ w = 1 \\ p = p_e \end{cases}\,. \tag{3e}$$

The first boundary condition, that of zero radial velocity on the axis, specifies that there are no sources or sinks there. The second sets the swirl ratio at the outer edge of the vortex, which characterizes the strength of the vortex. The third expresses the fact that velocities are nondimensionalized with respect to w_e; the fourth sets the edge pressure and can be arbitrarily chosen, since the quantities of interest, the pressure coefficients, will be independent of p_e.

For $n = 1$, these reduce to the inviscid conical equations of Hall [3]. The equations can be integrated exactly, yielding the following expressions for the radial, swirl and axial velocities, respectively:

$$u(\phi) = \frac{n\phi}{2}\left(1 - \sqrt{1 + 2{v_e}^2}\right) \tag{4a}$$

$$v(\phi) = \left[{v_e}^2 - \left(1 - \sqrt{1 + 2{v_e}^2}\right)^2 \ln\frac{\phi}{\phi_e}\right]^{1/2} \tag{4b}$$

$$w(\phi) = 1 + \left(1 - \sqrt{1 + 2{v_e}^2}\right)\ln\frac{\phi}{\phi_e}\,. \tag{4c}$$

The radial momentum equation, which for the slender vortex ($\phi \to 0$) reduces to a balance of pressure gradient and centripetal acceleration, is integrated separately, yielding the static pressure coefficient:

$$\begin{aligned} C_p &= \frac{p - p_e}{\frac{1}{2}\rho {w_e}^2} \\ &= 2{v_e}^2 \ln \frac{\phi}{\phi_e} - \left(1 - \sqrt{1 + 2{v_e}^2}\right)^2 \ln^2 \frac{\phi}{\phi_e} . \end{aligned} \tag{4d}$$

For growth rate $n > 0$ the radial velocity u is everywhere inward and is a linear function of ϕ. The radial velocity at any point also varies linearly in the growth rate n, assuming that v_e is held constant. It is interesting to note that the swirl and axial velocity distributions are independent of the growth rate of the vortex in this inviscid solution. Both have a log–like singularity on the axis, as does the pressure coefficient. It can be seen that for any finite edge pressure p_e the pressure actually becomes negative for small enough ϕ, a fact noted by Hall, who concluded that in a real vortex core, diffusion effects would invalidate the inviscid equations before this point were actually reached. The total pressure, which for a slender vortex is written as

$$\begin{aligned} p_0 &= p + \frac{1}{2}\left(v^2 + w^2\right) \\ &= p_e + \frac{1}{2}\left({v_e}^2 + 1\right) , \end{aligned} \tag{5}$$

(u^2 is negligible, since $u \propto \phi \ll 1$) is constant in the inviscid case, since there is no dissipation in the flow. Although the applicability of these equations to a real flow is limited, they do give a good qualitative idea of what happens in nearly irrotational regions outside the core of the leading–edge vortex, a fact which will become clear when these solutions are compared to solutions of the viscous equations.

1.4 A General Similarity Model for Viscous Incompressible Vortex Cores

Hall [3] and Stewartson and Hall [4] developed a model for the core of an incompressible leading-edge vortex by matching the conically ($n = 1$) self-similar, inviscid outer solution given by (4a-d) to a nonconical viscous inner solution of the form

$$w = W(z)\, f(\phi) , \tag{6a}$$

$$v = V(z)\, g(\phi) , \tag{6b}$$

where $\phi \propto r/z^{\frac{1}{2}}$ is the radial coordinate.

This inner solution corresponds roughly to parabolic ($n = 1/2$) growth in the general coordinates, but with a dependence on z as well as on the radial coordinate ϕ. Although the matching of the inner solution to an outer solution which ignores the presence of a viscous core means that the results are only approximate solutions of the Navier-Stokes equations, even in the limit as $Re \to \infty$, the solutions do show reasonably good agreement with the data of Earnshaw [1], but with a smaller core diameter and axial velocity peaks and pressure drops of larger magnitude than are seen experimentally.

The model of Powell and Murman [5] assumes steady flow, conical self–similarity and slenderness in the viscous limit as $Re \to \infty$, reducing the Navier-Stokes equations to a system of ordinary differential equations which are then solved numerically. The results are nearly identical to those of Hall, and form a one-parameter family of solutions. The parameter which characterizes the solutions is the maximum swirl velocity of the vortex, which is also taken to define the "edge" of the vortex core. The results lead to the conclusion that the level of total pressure loss in the core depends only on the strength of the vortex (as characterized by the maximum swirl velocity) and is independent of the Reynolds number. This has also been seen in other numerical solutions of the Euler and Navier-Stokes equations for leading–edge vortex flows [12, 9] and experiment [2].

Using the more general coordinates introduced previously, if derivatives in the ζ-direction are assumed to vanish and the viscous limit is considered, the equations of motion in nondimensional form reduce to the following set of ordinary differential equations, where (u, v, w) are the radial (r), azimuthal (θ) and axial (z) components of the velocity vector (still in cylindrical polar coordinates) and primes denote differentiation with respect to ϕ:

$$\frac{1}{z^n}\left(\frac{u}{\phi} + u'\right) - \left(\frac{n\phi}{z}\right) w' = 0 \tag{7a}$$

$$\left(\frac{u}{z^n}-\frac{n\phi w}{z}\right)u'-\frac{v^2}{\phi z^n} = -\frac{p'}{z^n} + \mathcal{D}(u)-\frac{1}{Re_z}\left(\frac{u}{\phi^2 z^{2n}}\right) \tag{7b}$$

$$\left(\frac{u}{z^n}-\frac{n\phi w}{z}\right)v'+\frac{uv}{\phi z^n} = \mathcal{D}(v)-\frac{1}{Re_z}\left(\frac{v}{\phi^2 z^{2n}}\right) \tag{7c}$$

$$\left(\frac{u}{z^n}-\frac{n\phi w}{z}\right)w' = -\frac{n\phi p'}{z}+\mathcal{D}(w)\ , \tag{7d}$$

where the differential operator $\mathcal{D}$ arises from the viscous terms and has the form:

$$\mathcal{D}=\frac{1}{Re_z}\left\{\left[\frac{n(n+1)\phi}{z^2}+\frac{1}{\phi z^{2n}}\right]\frac{\partial}{\partial\phi}+\left[\left(\frac{n\phi}{z}\right)^2+\frac{1}{z^{2n}}\right]\frac{\partial^2}{\partial\phi^2}\right\}\ , \tag{7e}$$

where the Reynolds number Re_z has the axial location as a reference length. The slenderness assumption together with the requirement that for self–similarity the equations must be independent of the axial location z leads to the following rescaling:

$$\tilde{\phi} = \frac{\phi\sqrt{Re_z}}{z^{1/2}}, \tag{8a}$$

$$\tilde{u} = \frac{u\sqrt{Re_z}}{z^{(1-2n)/2}}, \tag{8b}$$

$$\tilde{v} = \frac{v}{z^{1-2n}}, \tag{8c}$$

$$\tilde{w} = \frac{w}{z^{1-2n}}, \tag{8d}$$

$$\tilde{p} = \frac{p}{z^{2(1-2n)}}\ . \tag{8e}$$

The powers of z in the rescaling for ϕ cancel; if they did not, this would be inconsistent with the original self–similarity assumed. The swirl and axial velocity components v and w are scaled with the same power of z, so that the swirl ratio, a measure of the strength of the vortex, is invariant under the rescaling. The solutions sought thus are of the form

$$u_i = f_i(z)\,g_i\left(\tilde{\phi}\right)\ , \tag{9}$$

where u_i represents the vector of state variables (u,v,w,p) and the f_i are monomials in z. Note the resemblance of this equation to equation (6). In the limit as $Re_z\to\infty$, the resulting equations are, with primes now denoting differentiation with respect to $\tilde{\phi}$:

$$\frac{\tilde{u}}{\tilde{\phi}}+\tilde{u}'-n\tilde{\phi}\tilde{w}'=0 \tag{10a}$$

$$\tilde{p}'=\frac{\tilde{v}^2}{\tilde{\phi}} \tag{10b}$$

$$\tilde{v}''-\left(\tilde{u}-n\tilde{\phi}\tilde{w}-\frac{1}{\tilde{\phi}}\right)\tilde{v}'-\left(\tilde{u}+\frac{1}{\tilde{\phi}}\right)\frac{\tilde{v}}{\tilde{\phi}}=0 \tag{10c}$$

$$\tilde{w}''-\left(\tilde{u}-n\tilde{\phi}\tilde{w}-\frac{1}{\tilde{\phi}}\right)\tilde{w}'+n\tilde{v}^2=0\ , \tag{10d}$$

where the radial momentum equation (10b) has been used to eliminate the pressure term in the axial momentum equation (10d). The boundary conditions are:

$$\tilde{\phi}=0:\begin{cases}\tilde{u}=0\\ \tilde{v}=0\\ \tilde{w}'=0\end{cases}\ ,\qquad \tilde{\phi}=\tilde{\phi}_e:\begin{cases}\tilde{v}'=-\Gamma/\tilde{\phi}^2\\ \tilde{w}=1\\ \tilde{p}=p_e\end{cases}\ , \tag{11}$$

where the subscript e refers to the outer boundary set in the computation; the condition on the swirl velocity $\tilde{v}$ at $\tilde{\phi}_e$ is equivalent to a constant–circulation boundary condition. The other boundary conditions are much as in the inviscid case, but the viscous nature of the flow now imposes the additional requirement that the swirl velocity and the gradient of the axial velocity both vanish on the axis. It should be noted that by considering the more general case where the outer flow has a power–law dependence on the axial coordinate of the form $w_e = w_1 z^m$, it can be shown that the growth rate n should satisfy the relation:

$$n = \frac{1-m}{2} \ , \tag{12}$$

indicating that a self–similar incompressible vortex core in zero axial pressure gradient should grow as $z^{1/2}$, like a Blasius boundary layer. Most of the results presented are for this $n = 1/2$ case, although solutions with different values of n are useful because they illustrate what the effects of assuming a different rate of growth are and allow comparisons with the results of Powell and Murman ($n = 1$) and Hall ($n = 1$ for the outer solution.) However, (12) indicates that for values of n other than one–half, terms arising from a nonzero axial pressure gradient must be considered to obtain solutions that are self–similar in more than a "local" sense. The main advantages of the present approach lie in its generality and in the fact that the viscous core and inviscid outer flow are described by a single set of equations and are thus solved for in a coupled fashion.

It should be noted that there is one nontrivial case where an analytical result is easily obtained. For $n = 0$ the vortex is columnar, i.e. the core does not grow with z. In this case the viscous equations can be immediately integrated, the result being that the only steady solution for a viscous vortex with zero growth rate is a solid–body rotation with constant axial velocity and zero radial velocity.

The three coupled equations (10a,c,d) are rewritten as a set of five first-order equations, discretized using central differences and solved using a box scheme and a Newton iteration procedure. The radial momentum equation (10b) is then integrated separately to obtain the pressure distribution. At a given value of the outer–boundary circulation, convergence to double-precision machine zero typically takes only five or six iterations, on a grid fine enough to provide a mesh–converged solution. Because the maximum swirl velocity (taken to define the edge of the core) in the vortex is part of the solution, the solution algorithm iterates on the circulation until the desired $\tilde{v}_{max}$ is reached in the converged solution.

Results for the parabolic ($n = 1/2$) vortex are presented in Figures 1–6. Figures 1, 2 and 3 show swirl($\tilde{v}$), axial($\tilde{w}$) and radial($\tilde{u}$) velocity distributions for three different maximum swirl velocity values. The swirl velocity distributions reveal a solid–body rotation in the core, reaching a maximum and joining smoothly to a constant–circulation velocity distribution farther out. The axial velocity profiles show a jet–like overshoot on the axis which is quite pronounced at higher swirl velocities. The radial velocity is everywhere negative, or inward, and is nearly linear away from the axis, going smoothly to zero as the axis is reached. It is evident that all three scaled velocity components are the same order of magnitude, as desired. The figures show that as the swirl velocity of the vortex becomes larger (i.e. the strength of the vortex increases,) the axial velocity in the core increases markedly, as does the magnitude of the radial velocity, indicating that the rate of entrainment of fluid into the core is increasing. For comparison, the inviscid solutions corresponding to the $\tilde{v}_{max} = 1$ case are plotted and are represented by the dashed lines in the figures. It can be seen that outside of the core region, that is, for $\tilde{\phi} > \tilde{\phi}(\tilde{v}_{max})$, the solution is essentially inviscid. Figures 4 and 5 show the static and total pressure distributions, with the static pressure coefficient C_p and total pressure coefficient C_h defined as:

$$C_p = \frac{p - p_\infty}{\frac{1}{2}\rho w_e^2} \ , \qquad C_h = \frac{p_0 - p_{0\infty}}{\frac{1}{2}\rho w_e^2} \ , \tag{13}$$

where the subscript e refers to $\tilde{\phi}_e$, the outer boundary set in the computation; the pressure p_∞ is found by integrating equation (10b) from $\tilde{\phi}_e$ to infinity for a constant–circulation outer flow. The solutions show that the static pressure loss on the axis increases as $\tilde{v}_{max}$ increases; the total pressure loss in the core increases quadratically with $\tilde{v}_{max}$. The scaled axial component of vorticity is defined as

$$\tilde{\omega}_z = \left(\tilde{v}' + \frac{\tilde{v}}{\tilde{\phi}} \right) \ , \tag{14}$$

and is plotted in Figure 6. The vorticity is high in a narrow region near the axis and drops off rapidly farther out. The inviscid solutions corresponding to $\tilde{v}_{max} = 1$ are again plotted as dashed lines for comparison in these figures.

To see what happens when different rates of growth of the core are assumed, results for a range of n are presented in Figures 7–10. It can be seen that increasing n (thus increasing the assumed local rate of growth of the core at a

given axial location) actually results in a smaller core radius. It should be stressed that varying the parameter n is of mathematical interest but not an effect which would be seen physically for these types of flows; a real vortex would require the presence of an axial pressure gradient or some other mechanism to change the growth rate.

Increasing n also increases the axial velocity surplus, the radial inflow velocity and the level of core static pressure loss. However, the level of *total* pressure loss in the core is independent of n and the Reynolds number as $Re_z \rightarrow \infty$ (though its distribution is not.) This means that the core total pressure loss for a viscous vortex of arbitrary growth rate depends only on the edge swirl velocity of the vortex, and is independent of the level of diffusion in the core, a fact also noted by Powell [9] in Euler computations of leading–edge vortices having varying levels of artificial viscosity.

Finally, Figures 11-13 compare both the conical results of Powell and Murman and the present results for the $n = 1/2$ vortex to the experimental data of Earnshaw [1]. The experimental data points shown correspond to horizontal and vertical traverses of five–hole probe at 70–percent chord of a delta wing at a 14.9 degree angle of attack. For both Hall's and Powell and Murman's conical solutions, the axial velocity surplus and the core static pressure loss were overpredicted and the core radius underpredicted in comparison with Earnshaw's data. The parabolic vortex model improves the velocity and pressure predictions as well as resulting in a somewhat more diffuse core. However, the core diameter is still slightly underpredicted when compared to experiment, most likely due to the assumption of laminar flow in the present model. Earnshaw's experimental results are for a Reynolds number of approximately a quarter–million, indicating that there was most likely some turbulent diffusion in the experimental flows studied.

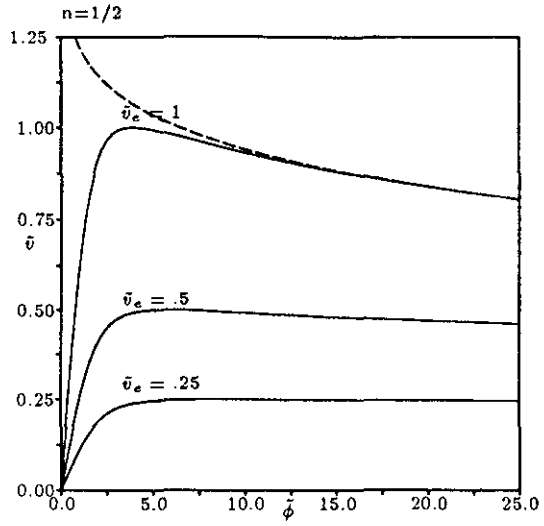

Figure 1: Incompressible vortex – Swirl Velocity Distributions

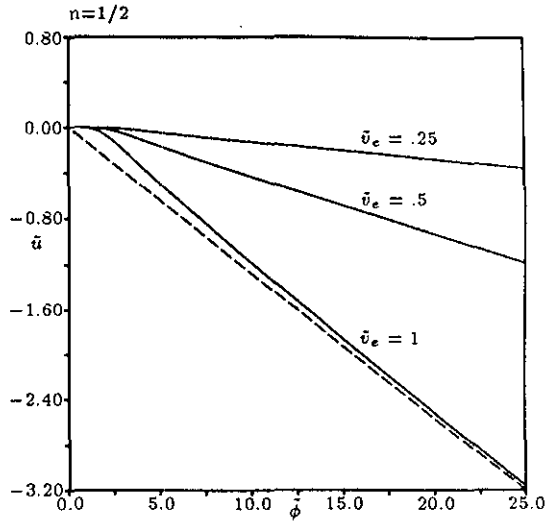

Figure 3: Incompressible vortex – Radial Velocity Distributions

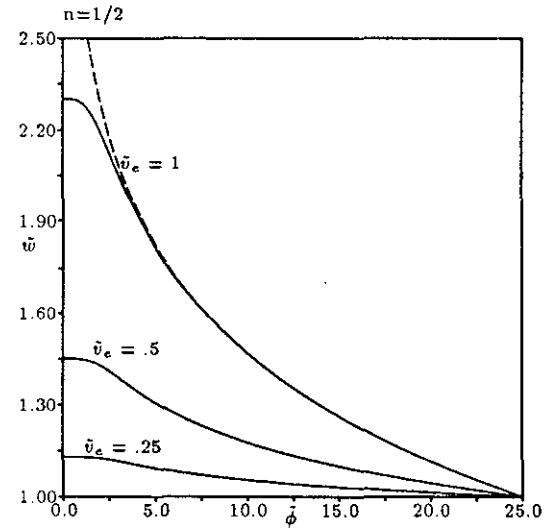

Figure 2: Incompressible vortex – Axial Velocity Distributions

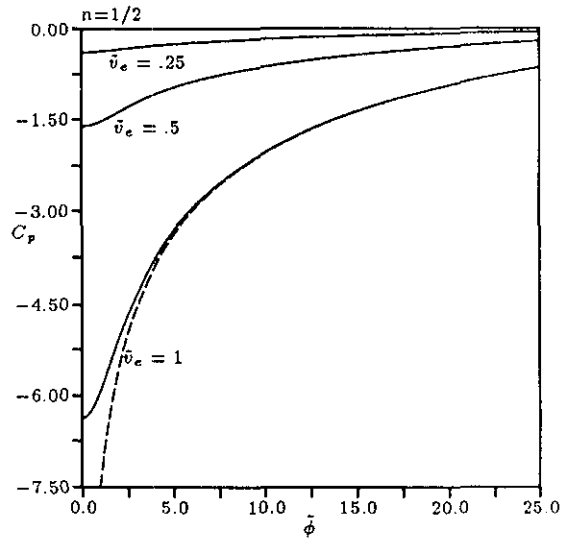

Figure 4: Incompressible vortex – Static Pressure Distributions

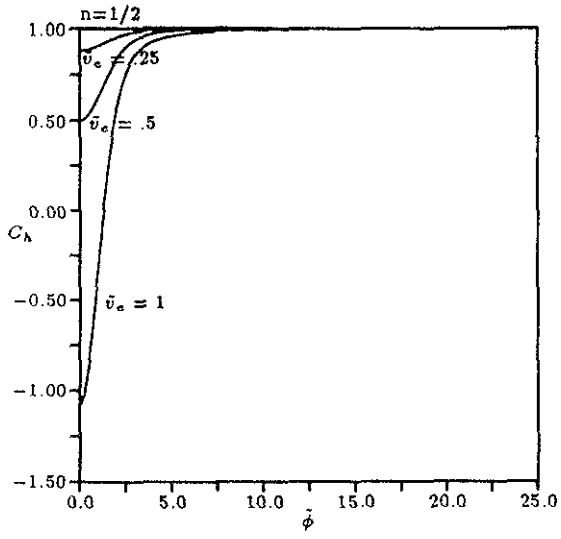

Figure 5: Incompressible vortex – Total Pressure Distributions

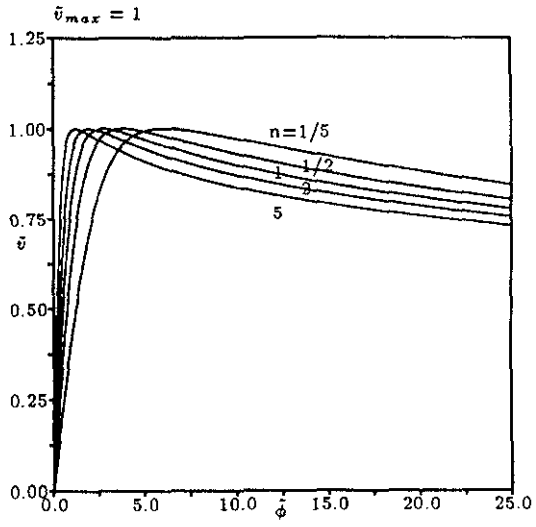

Figure 7: Incompressible Vortex – Swirl Velocity Distributions for various rates of growth

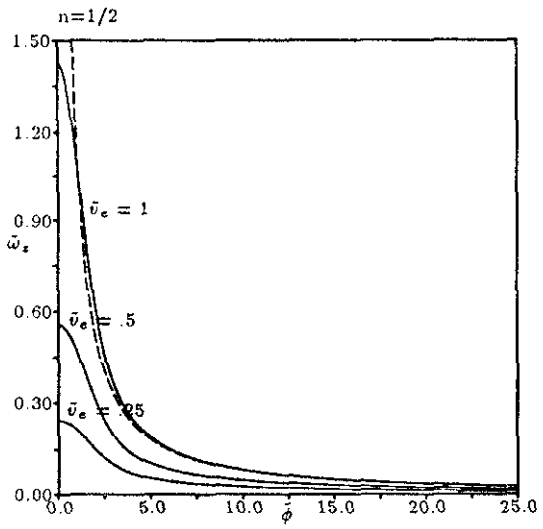

Figure 6: Incompressible vortex – Vorticity Distributions

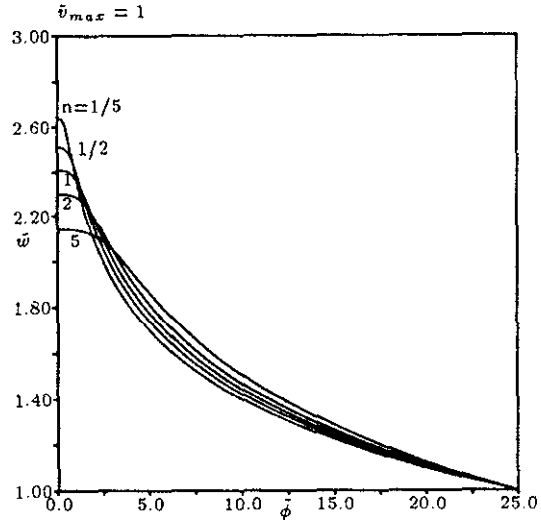

Figure 8: Incompressible Vortex – Axial Velocity Distributions for various rates of growth

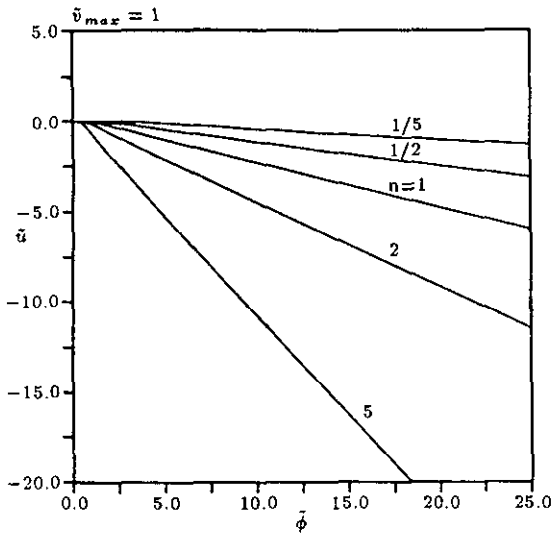

Figure 9: Incompressible Vortex – Radial Velocity Distributions for various rates of growth

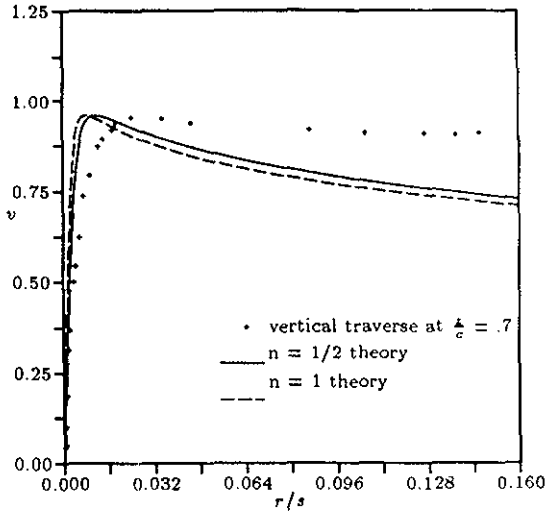

Figure 11: Comparison with Earnshaw — Swirl Velocity Distributions

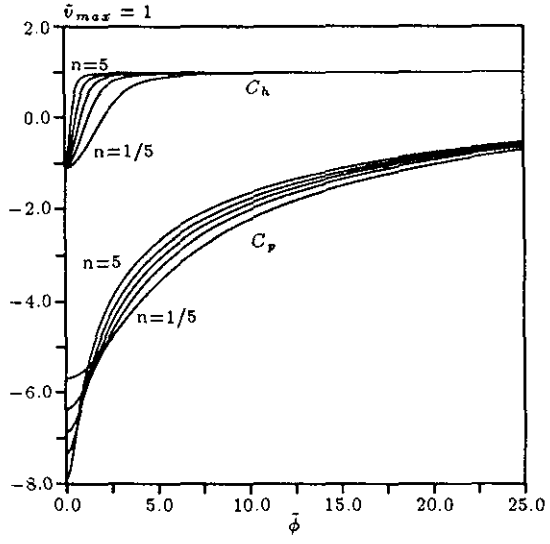

Figure 10: Incompressible Vortex – Static and Total Pressure Distributions for various rates of growth

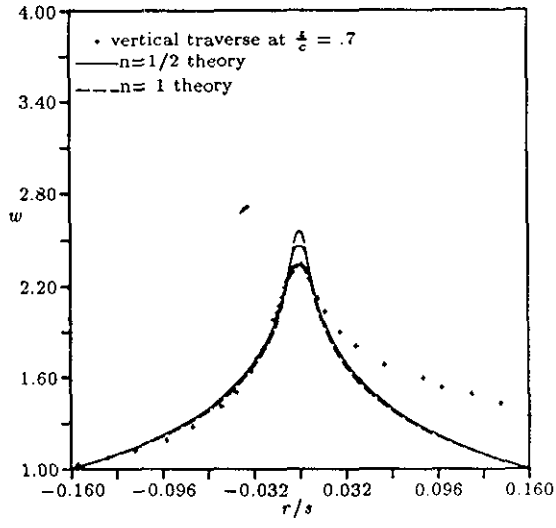

Figure 12: Comparison with Earnshaw — Axial Velocity Distributions

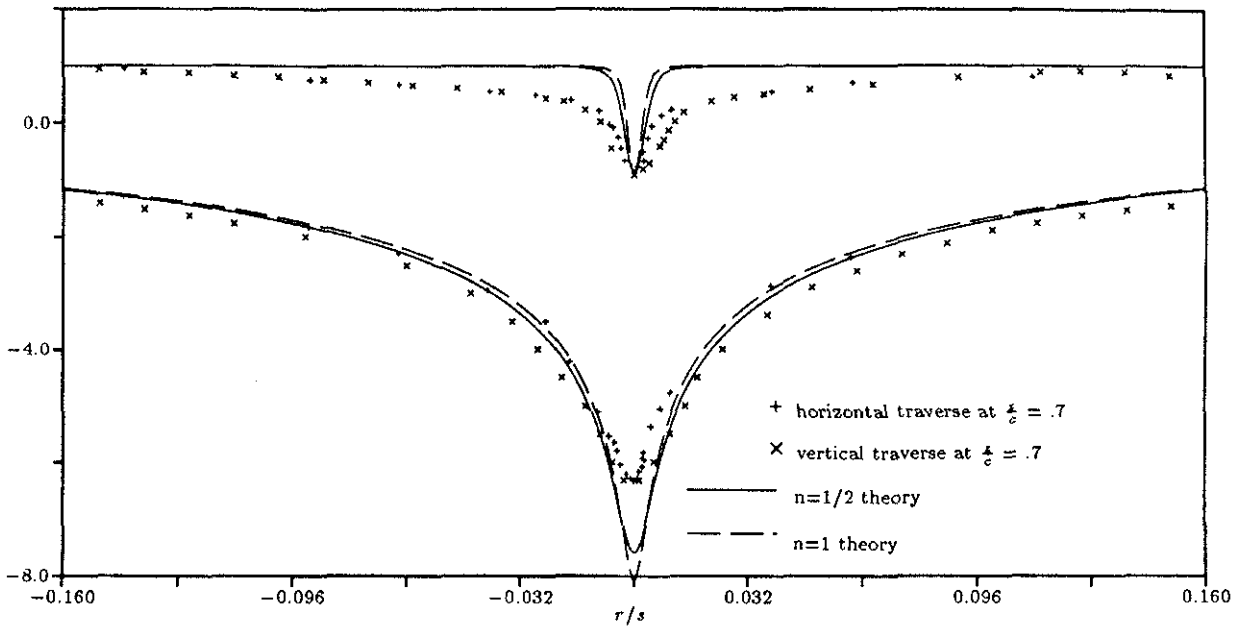

Figure 13: Comparison with Earnshaw — Static and Total Pressure Distributions

1.5 Rate of Growth of a Vortex Core in Zero Axial Pressure Gradient

Many of the similarity models mentioned so far assume conical similarity, i.e. a linear growth rate for the vortex core, because in the case of a leading-edge vortex,the shear layer rolling up over a wing with constant sweep angle grows in a roughly conical fashion. However, the experimental results of Earnshaw [1] and some simple analytical arguments predict that the viscous inner core of the vortex should grow with the square root of the distance from its apex at high Reynolds number, much like an incompressible boundary layer in zero pressure gradient. This can be seen through the following arguments: in the equations of motion (1) in the original cylindrical polar coordinates, a slenderness assumption may be made by scaling the r-coordinate

$$r = \epsilon \tilde{r} \qquad \epsilon \ll 1 \,. \tag{15a}$$

Substituting this relation into the continuity equation leads to the same scaling for the radial velocity:

$$u = \epsilon \tilde{u} \,. \tag{15b}$$

The remaining dependent and independent variables remain unchanged, i.e.

$$v = \tilde{v}, \;\; w = \tilde{w}, \;\; p = \tilde{p}, \;\; z = \tilde{z}. \tag{15c}$$

Dropping higher-order terms in ϵ and assuming zero axial pressure gradient, the rescaled equations of continuity and conservation of momentum are:

$$\frac{1}{\tilde{r}}\frac{\partial}{\partial \tilde{r}}(\tilde{r}\tilde{u}) + \frac{\partial \tilde{w}}{\partial \tilde{z}} = 0 \tag{16a}$$

$$\frac{\partial \tilde{p}}{\partial \tilde{r}} - \frac{\tilde{v}^2}{\tilde{r}} = \frac{1}{Re_{\tilde{z}}}\left[\frac{1}{\tilde{r}}\frac{\partial}{\partial \tilde{r}}\left(\tilde{r}\frac{\partial \tilde{u}}{\partial \tilde{r}}\right) - \frac{\tilde{u}}{\tilde{r}^2}\right] \tag{16b}$$

$$\tilde{u}\frac{\partial \tilde{v}}{\partial \tilde{r}} + \tilde{w}\frac{\partial \tilde{v}}{\partial \tilde{z}} + \frac{\tilde{u}\tilde{v}}{\tilde{r}} = \frac{1}{\epsilon^2 Re_{\tilde{z}}}\left[\frac{1}{\tilde{r}}\frac{\partial}{\partial \tilde{r}}\left(\tilde{r}\frac{\partial \tilde{v}}{\partial \tilde{r}}\right) - \frac{\tilde{v}}{\tilde{r}^2}\right] \tag{16c}$$

$$\tilde{u}\frac{\partial \tilde{w}}{\partial \tilde{r}} + \tilde{w}\frac{\partial \tilde{w}}{\partial \tilde{z}} = \frac{1}{\epsilon^2 Re_{\tilde{z}}}\left[\frac{1}{\tilde{r}}\frac{\partial}{\partial \tilde{r}}\left(\tilde{r}\frac{\partial \tilde{w}}{\partial \tilde{r}}\right)\right] \tag{16d}$$

The continuity equation remains invariant under the scaling. The radial momentum equation, for high Reynolds number, reduces to a balance of radial pressure gradient and centripetal acceleration. The θ and z-momentum equations show that, for a balance of convective and viscous terms (a criterion which can be used to define the edge of the core), the scaling variable ϵ must satisfy

$$\epsilon \propto \frac{1}{\sqrt{Re_z}} \propto \frac{1}{\sqrt{z}} . \tag{17}$$

This implies that

$$r_{edge} \propto \sqrt{z} , \tag{18}$$

implying that the core of a slender, viscous, incompressible vortex should grow as $z^{1/2}$. It is interesting that numerical evidence for this can be found even from the conical model, keeping in mind that the assumption here is one of local, not global, conical similarity. If higher-order terms in $1/Re_z$ are retained in the equations of Powell and Murman [5], the effect of finite Reynolds number on both core location and the velocity field can be examined. The results show that for Reynolds numbers as low as $Re_z = \mathcal{O}(10^2)$, the core locations in the scaled coordinate $\tilde{\phi}$ (which is proportional to $r/\sqrt{z}$) are virtually indistinguishable. This can also be seen by examining the leading error terms in the above equations, which are all $\mathcal{O}({Re_z}^{-1})$. The finite Reynolds number solutions also show that the core axial velocity and the magnitude of the core static pressure drop are both reduced with decreasing Reynolds number, in agreement with the qualitative predictions of Hall [3]. The radial velocity magnitude also decreases with decreasing Re_z, and the core diameter, which is normalized with ${Re_z}^{1/2}$, begins to increase, indicating that the core grows at a rate greater than $z^{1/2}$ at low Reynolds numbers.

2 Similarity Models for Compressible Vortex Cores

Very little theoretical work on viscous compressible vortex cores has been done to date. One main area of interest is the effect of compressibility on the flowfield vis-a-vis the incompressible case. Hall [8] mentions that the main effect of compressibility on the velocity field is a "radical change in the responsiveness of the internal core structure to changes in conditions on the outside of the core," but demonstrates this only in a qualitative sense. The fact that a vortex over a given lifting surface in compressible flow may have a completely different structure than at low speeds has significant implications for slender wing configurations, where the upper–surface flow may be dominated by the vortices rolling up from the leading edge. The presence of compressibility may lead to extremely low densities and pressures in the vicinity of the axis of the vortex. Solutions to the inviscid equations of motion show that the density in the core can go to zero; as the swirl velocity or the Mach number is increased from this point the region of vacuum becomes larger. Whether the presence of viscosity prevents the density from actually reaching a vacuum is a question which solutions of the full equations of motion will address.

Another interesting phenomenon which appears in connection with compressibility is the energy separation or "Ranque–Hilsch" effect, where the presence of viscosity in a compressible flow with curved streamlines leads, in general, to non-constant stagnation enthalpy in the flow. This limits the usefulness of a boundary–layer analogy such as was used in the incompressible case – in a compressible flow the boundary layer flow (assuming no wall heat transfer,) having little curvature, has essentially constant stagnation enthalpy but the vortex does not. Instead, there is a complicated balance of dissipative heating, cooling through core expansion and heat transfer between the core and the outer flow, the combination of which can lead to significant temperature gradients in the core of the vortex, as will be shown.

As with the incompressible core, the approach will be to look at the less complicated inviscid cases before moving on to the full viscous equations of motion.

2.1 Governing Equations

In cylindrical polar (r, θ, z) coordinates, the equations expressing conservation of mass, momentum and energy for the steady, axisymmetric flow of a viscous, heat–conducting gas are, with ρ, u, v, w and T denoting density, radial, azimuthal and axial components of velocity and the static temperature of the flow, respectively:

$$\frac{1}{r}\frac{\partial(r\rho u)}{\partial r} + \frac{\partial(\rho w)}{\partial z} = 0 \ , \tag{19a}$$

$$\rho\left(u\frac{\partial u}{\partial r}+w\frac{\partial u}{\partial z}-\frac{v^2}{r}\right)=-\frac{\partial p}{\partial r}+\mu\left[\frac{\partial}{\partial r}\left(\frac{1}{r}\frac{\partial(ru)}{\partial r}\right)+\frac{\partial^2 u}{\partial z^2}\right]+\frac{\mu}{3}\frac{\partial}{\partial r}\left[\frac{1}{r}\frac{\partial(ru)}{\partial r}+\frac{\partial w}{\partial z}\right]$$
$$+\frac{2}{3}\frac{\partial\mu}{\partial r}\left[2\frac{\partial u}{\partial r}-\frac{u}{r}-\frac{\partial w}{\partial z}\right]+\frac{\partial\mu}{\partial z}\left(\frac{\partial w}{\partial r}+\frac{\partial u}{\partial z}\right)\ , \tag{19b}$$

$$\rho\left(u\frac{\partial v}{\partial r}+w\frac{\partial v}{\partial z}+\frac{uv}{r}\right)=\mu\left[\frac{\partial}{\partial r}\left(\frac{1}{r}\frac{\partial(rv)}{\partial r}\right)+\frac{\partial^2 v}{\partial z^2}\right]+\frac{\partial\mu}{\partial r}\left[r\frac{\partial}{\partial r}\left(\frac{v}{r}\right)\right]+\frac{\partial\mu}{\partial z}\frac{\partial v}{\partial z}\ , \tag{19c}$$

$$\rho\left(u\frac{\partial w}{\partial r}+w\frac{\partial w}{\partial z}\right)=-\frac{\partial p}{\partial z}+\mu\left[\frac{1}{r}\frac{\partial}{\partial r}\left(r\frac{\partial w}{\partial r}\right)+\frac{\partial^2 w}{\partial z^2}\right]+\frac{\mu}{3}\frac{\partial}{\partial z}\left[\frac{1}{r}\frac{\partial(ru)}{\partial r}+\frac{\partial w}{\partial z}\right]$$
$$+\frac{\partial\mu}{\partial r}\left(\frac{\partial w}{\partial r}+\frac{\partial u}{\partial z}\right)-\frac{2}{3}\frac{\partial\mu}{\partial z}\left[\frac{1}{r}\frac{\partial(ru)}{\partial r}-2\frac{\partial w}{\partial z}\right]\ , \tag{19d}$$

$$\rho C_p\left(u\frac{\partial T}{\partial r}+w\frac{\partial T}{\partial z}\right)+\frac{T}{\rho}\left(\frac{\partial\rho}{\partial T}\right)_{p=const.}\left(u\frac{\partial p}{\partial r}+w\frac{\partial p}{\partial z}\right)=k\left[\frac{1}{r}\frac{\partial}{\partial r}\left(r\frac{\partial T}{\partial r}\right)+\frac{\partial^2 T}{\partial z^2}\right]+\frac{\partial k}{\partial r}\frac{\partial T}{\partial r}+\frac{\partial k}{\partial z}\frac{\partial T}{\partial z}$$
$$+\mu\left\{2\left[\left(\frac{\partial u}{\partial r}\right)^2+\left(\frac{u}{r}\right)^2+\left(\frac{\partial w}{\partial z}\right)^2\right]+\left[r\frac{\partial}{\partial r}\left(\frac{v}{r}\right)\right]^2+\left(\frac{\partial w}{\partial r}+\frac{\partial u}{\partial z}\right)^2+\left(\frac{\partial v}{\partial z}\right)^2-\frac{2}{3}\left[\frac{1}{r}\frac{\partial(ru)}{\partial r}+\frac{\partial w}{\partial z}\right]^2\right\}\ , \tag{19e}$$

where μ, C_p and k are the viscosity, specific heat at constant pressure and thermal conductivity, respectively. If μ, C_p and k are specified as functions of the flow variables then the perfect gas law $p \propto \rho T$ closes the equations. In most instances the gas is also assumed to satisfy a polytropic relation $p \propto \rho^\gamma$, where γ is the ratio of specific heats of the gas. This results in the simple expression $c^2 = \gamma p \rho^{-1}$ for the sound speed c. The viscosity μ is generally only a function of temperature which can be accurately modeled using Sutherland's law or, more simply, a power–law relation; in many cases the Prandtl number ($Pr = \mu C_p k^{-1}$, a nondimensional combination of the transport coefficients of the gas) is taken to be constant. The above equations form a system of coupled, nonlinear partial differential equations whose type depends on the local flow conditions, so it is desirable to seek some simplification which makes the solution of the equations more tractable but still preserves the fundamental physics of the flow. The following sections look at successive levels of approximation to these equations and the insights which can be gained from each.

2.2 Results from Potential–Flow Theory

The most drastic simplification of equations (19) which still gives nontrivial solutions is obtained by considering a steady, irrotational inviscid flow. In this case the equations of motion reduce to the following:

$$\frac{1}{r}\frac{\partial(r\rho u)}{\partial r}+\frac{\partial(\rho w)}{\partial z}=0 \tag{20a}$$

$$\rho\left(u\frac{\partial u}{\partial r}+w\frac{\partial u}{\partial z}-\frac{v^2}{r}\right)=-\frac{\partial p}{\partial r} \tag{20b}$$

$$\rho\left(u\frac{\partial v}{\partial r}+w\frac{\partial v}{\partial z}+\frac{uv}{r}\right)=0 \tag{20c}$$

$$\rho\left(u\frac{\partial w}{\partial r}+w\frac{\partial w}{\partial z}\right)=-\frac{\partial p}{\partial z}. \tag{20d}$$

Irrotationality imposes the additional constraint that

$$\omega=\left(-\frac{\partial v}{\partial z}\right)\mathbf{e_r}+\left(\frac{\partial u}{\partial z}-\frac{\partial w}{\partial r}\right)\mathbf{e}_\theta+\left(\frac{\partial v}{\partial r}+\frac{v}{r}\right)\mathbf{e_z}=0\ , \tag{21}$$

where ω is the vorticity vector and $\mathbf{e_r}, \mathbf{e}_\theta$ and $\mathbf{e_z}$ are the unit vectors relative to cylindrical polar coordinates. It is immediately apparent that the swirl velocity should satisfy the following relation:

$$v=\frac{\Gamma}{r}\ , \tag{22}$$

where the circulation Γ is a constant of the flow. This satisfies both irrotationality and the θ–momentum equation (20c). The pressure terms in the above equations can be eliminated by combining (20b) and (20d), and after some manipulation the following set of equations expressing conservation of mass, momentum and irrotationality results:

$$\frac{\rho u}{r} + \frac{\partial(\rho u)}{\partial r} + \frac{\partial(\rho w)}{\partial z} = 0 \tag{23a}$$

$$\frac{\partial \rho}{\partial z}\left[\frac{\partial}{\partial r}\left(u^2 + w^2\right)\right] = \frac{\partial \rho}{\partial r}\left[\frac{\partial}{\partial z}\left(u^2 + w^2\right)\right] \tag{23b}$$

$$\frac{\partial u}{\partial z} = \frac{\partial w}{\partial r} \ . \tag{23c}$$

It is straightforward to show that under the simplifying assumption that a separation of variables is possible, i.e. that

$$u(r,z) = \tilde{u}(r)\,U(z) \tag{24a}$$

$$w(r,z) = \tilde{w}(r)\,W(z) \tag{24b}$$

$$\rho(r,z) = \tilde{\rho}(r)\,R(z)\,, \tag{24c}$$

the only admissible solution is one having $u = 0$, $w = w_\infty$ and $\rho = \rho(r)$. Thus the solutions sought describe flowfields having zero radial velocity and constant axial velocity; density, pressure and swirl velocity are functions of the radial coordinate only. If the density in the limit $r \to \infty$ is denoted by ρ_∞, then the radial momentum equation (20b) can be integrated, again using the polytropic gas relation, giving:

$$\frac{\rho}{\rho_\infty} = \left[1 - \left(\frac{\gamma - 1}{2}\right)\frac{\Gamma^2}{{c_\infty}^2 r^2}\right]^{\frac{1}{\gamma - 1}} \ . \tag{25}$$

Since $\rho \geq 0$ everywhere, there is a limiting radius where the density vanishes, given by

$$r_{lim} = \Gamma M_\infty \sqrt{\frac{\gamma - 1}{2}} \ , \tag{26}$$

where M_∞ is the Mach number at infinity. Thus the irrotational compressible vortex has a vacuum core whose diameter is proportional to the product of the circulation Γ and the Mach number M_∞. It can be shown that at the limiting radius, the pressure and temperature also go to zero. The Mach number there becomes unbounded but the swirl velocity reaches a limiting value:

$$v_{lim} = \frac{1}{M_\infty}\sqrt{\frac{2}{\gamma - 1}} \ . \tag{27}$$

This stands in contrast to the incompressible case, where the velocities are singular on the axis, and is to be expected since in compressible flow the internal energy of the fluid is assumed to be finite. The Mach number going to infinity merely indicates that at the limiting radius, the flow has been fully expanded, i.e. all of its internal energy has been converted into kinetic energy, resulting in a velocity which is finite.

2.3 The Inviscid Rotational Compressible Vortex

Following the solutions of Hall for incompressible vortices, Brown [6] formulated an inviscid model for a rotational, conically self–similar compressible vortex core. The flow was taken to be both isentropic and isenthalpic. Under these assumptions, the governing equations reduce to a set of ordinary differential equations in the radial coordinate. The equations were rewritten so that a single equation was obtained for the density (with the axial velocity as the independent coordinate) and solved using a semi-inverse method. As a result of the solution method, the solutions obtained were all for the case where the density vanishes just as the axis is reached.

Brown's solutions showed that for the rotational inviscid vortex the swirl velocity goes to zero on the axis and that the axial velocity is finite there as well (though with infinite gradient). Both quantities become singular on the axis for an incompressible inviscid vortex, so Brown concluded that compressibility appears to have a regularizing effect on the velocity field, much like that of a viscous boundary layer.

To allow a detailed examination of the inviscid equations and a comparison with the solutions of the viscous equations which will follow, the equations for steady, inviscid, rotational axisymmetric flow are nondimensionalized

with axial velocity and density at the outer edge of the region of interest and written in terms of conical similarity coordinates, a special case of the general coordinates introduced in Section 1.2, having $n = 1$. This leads to the following set of equations:

$$\text{Mass}: \quad -\phi\left[\rho\left(w-\frac{u}{\phi}\right)\right]' + \frac{2\rho u}{\phi} = 0 \tag{28a}$$

$$r-\text{momentum}: \quad \phi\left(w-\frac{u}{\phi}\right)u' + \frac{v^2}{\phi} = \frac{p'}{\rho} \tag{28b}$$

$$\theta-\text{momentum}: \quad \phi\left(w-\frac{u}{\phi}\right)v' - \frac{uv}{\phi} = 0 \tag{28c}$$

$$z-\text{momentum}: \quad \phi\left(w-\frac{u}{\phi}\right)w' = -\phi\frac{p'}{\rho}\ . \tag{28d}$$

Assuming slenderness eliminates the u and w terms from the radial momentum equation, reducing it to a balance of pressure gradient and centripetal acceleration; the other equations are unchanged. The polytropic gas relation is used to express the pressure derivatives in terms of the density and the ratio of specific heats γ. The isentropic assumption means that the energy equation is automatically satisfied. This leaves a system of four equations for the density ρ and the three velocity components u, v and w. The boundary conditions are the following:

$$\phi = 0: \ u = 0\ , \qquad \phi = \phi_e: \begin{cases} \rho = 1 \\ v = v_e \\ w = 1 \end{cases}\ , \tag{28e}$$

The equations are discretized as described in Section 1.4 and solved numerically. These equations are the same equations that Brown solved, with the important difference that the present solution procedure does not suffer from the restriction that density should vanish on the axis. The numerical solution procedure of Section 1.4 is modified so that the iteration occurs only where the density is nonzero, since the Jacobian matrix used in the iteration is singular in regions of vacuum.

Results are presented in figures 14-17, for an edge swirl velocity of unity. It can be seen that at low Mach numbers ($M_\infty = .1$), the density remains nonzero everywhere and the swirl velocity v does not drop to zero on the axis but reaches a finite value there (although the gradient is high). At slightly higher Mach numbers ($M_\infty = .2$), the swirl velocity again rises from its outer boundary value, but curves downward as the axis is approached. Increasing the Mach number further causes this drop in swirl velocity to become more pronounced, but the value on the axis does not become zero until the density there vanishes also, which happens at $M_\infty = .366$. This means that the zero swirl velocity on the axis seen by Brown is only for the special class of solutions where the density also goes to zero there. Further increases of the Mach number cause the region of vacuum to expand outward, and the gradients of axial and swirl velocity at the point where the density vanishes are now zero.

Another interesting result is that, as the Mach number is increased (for a given edge swirl velocity), the magnitude of the axial velocity peak and the drop in static pressure coefficient both decrease. This indicates that conditions in the vortex core become less sensitive to changes on the outside, in agreement with the predictions of Hall [8]. The radial velocity, which is nonpositive everywhere for both the inviscid and viscous incompressible vortex, shows regions of positivity as the Mach number increases, which means that the core is expanding. The entrainment velocity $u - n\phi w$, however, is still negative everywhere, as it should be for a self-similar flow with positive growth rate.

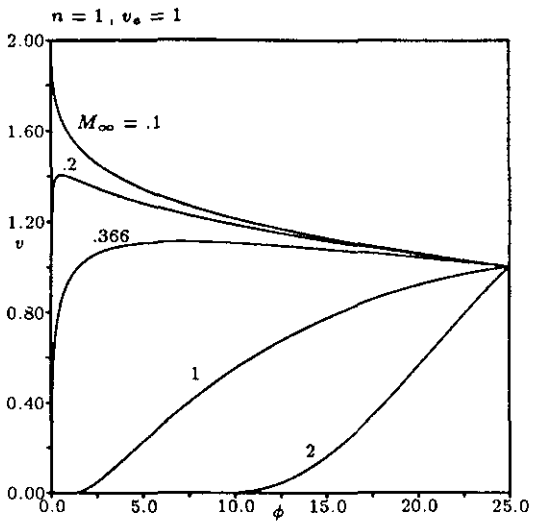

Figure 14: Inviscid Compressible vortex — Swirl Velocity Distributions

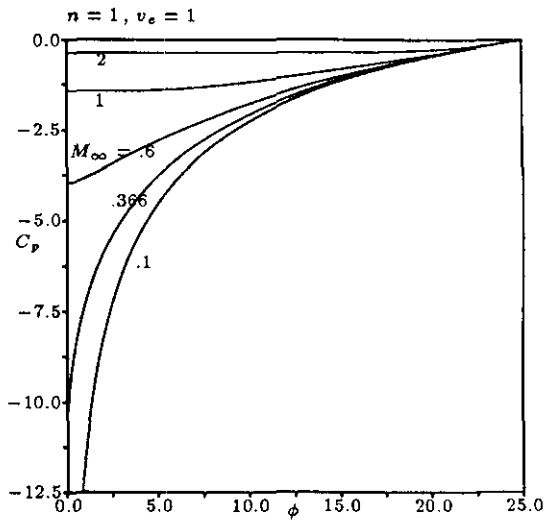

Figure 16: Inviscid Compressible vortex — Static Pressure Distributions

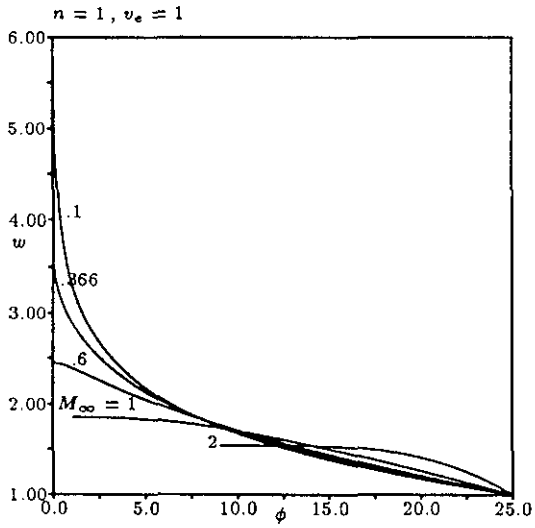

Figure 15: Inviscid Compressible vortex — Axial Velocity Distributions

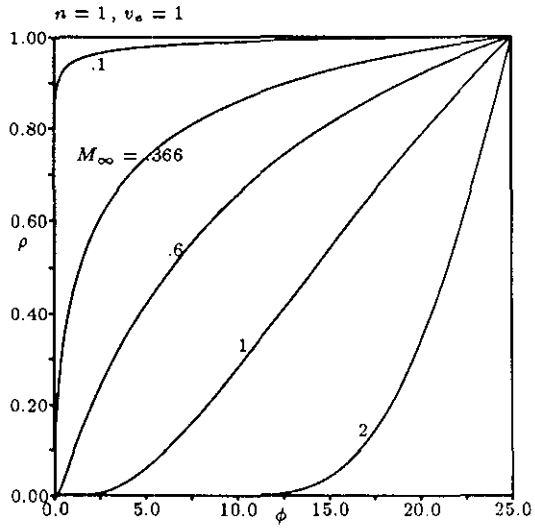

Figure 17: Inviscid Compressible vortex — Density Distributions

One feature of the solutions which is left unexplained by Brown is what happens at the outer computational boundary at Mach numbers greater than unity. It is clear from the figures that as M_∞ increases, gradients of axial and swirl velocity and density at the outer boundary become larger and larger. Brown's original solutions showed that as $M_\infty \rightarrow \infty$, the axial velocity jumps up to some value greater than unity and the swirl velocity and density drop to zero, all in the immediate vicinity of the outer boundary, making any kind of a smooth match to some outer flow seem unlikely, if not impossible. It should be noted that Brown's solutions are all for a swirl ratio (ratio of swirl to axial velocity at the outer boundary of the flowfield) of unity. However, a high Mach number implies that even a swirl–free flow is already near the limiting velocity mentioned in the previous section, which indicates that an additional swirl velocity yielding a swirl ratio of one is physically unachievable. Since the numerical procedure has no way of distinguishing between physically attainable and nonphysical solutions, an analytical estimate of the limiting swirl velocity for given conditions at the outer boundary is needed.

2.4 Limiting Velocity for the Compressible Vortex

Consider some point in a compressible flow at which the sound speed is c and the Mach number (based on the magnitude of the velocity vector) is M. The limiting velocity for this point in the flow is given by

$$q_{max}^2 = \left(\frac{2}{\gamma - 1}\right) {c_0}^2, \tag{29}$$

where c_0 denotes the stagnation sound speed, related to c by

$$\frac{c_0^2}{c^2} = 1 + \frac{\gamma - 1}{2} M^2. \tag{30}$$

In a quasicylindical or slender vortical flow, the radial velocity is negligible. Letting the subscript e denote conditions at the outer boundary or "edge" of the vortex and basing the Mach number M_z on the axial component of velocity w, the magnitude of the velocity is:

$${q_e}^2 = {v_e}^2 + {w_e}^2 = \left[\left(\frac{v_e}{w_e}\right)^2 + 1\right] {M_{ze}}^2 {c_e}^2 . \tag{31}$$

Dividing by ${q_{max}}^2$ gives

$$\begin{aligned} \left(\frac{q}{q_{max}}\right)^2 &= \frac{\gamma - 1}{2} {M_{ze}}^2 \left[\left(\frac{v_e}{w_e}\right)^2 + 1\right] \frac{{c_e}^2}{{c_{0e}}^2} \\ &= \frac{\frac{\gamma-1}{2} {M_{ze}}^2}{1 + \frac{\gamma-1}{2} {M_{ze}}^2} \left[\left(\frac{v_e}{w_e}\right)^2 + 1\right] \leq 1 , \end{aligned} \tag{32}$$

yielding the following constraint on the edge swirl ratio:

$$\frac{v_e}{w_e} \leq \frac{1}{M_{ze}} \sqrt{\frac{2}{\gamma - 1}} . \tag{33}$$

This is essentially the same as expression for the limiting velocity as was found for the irrotational compressible vortex. For $\gamma = 1.4$, this indicates that Brown's solutions for the inviscid compressible vortex (where solutions are shown for $\frac{v_e}{w_e} = 1$) can only be considered physically valid for $M_\infty \leq \sqrt{5}$. It should also be noted that if the limiting–velocity criterion is satisfied at the outer boundary of the domain of interest, then conservation of energy ensures that it will be satisfied everywhere in the interior of this domain.

2.5 The Viscous Compressible Vortex

To get a good idea of how a real compressible vortex behaves it is necessary to include the effects of viscosity and nonconstant stagnation enthalpy. To this end, a similarity model based on the compressible, viscous equations of motion has been developed. The steady, axisymmetric Navier-Stokes equations in cylindrical polar coordinates are nondimensionalized with respect to the density, axial velocity, temperature and viscosity at some reference point

(taken to be the outer boundary of the computational domain). Constant specific heats and thermal conductivity are assumed; the perfect gas law closes the equations. The general coordinate transformation is performed and similarity is assumed. The variables are rescaled as in the incompressible case, with the addition of the temperature, which is rescaled as:

$$\tilde{T} = \frac{T}{(\gamma - 1) {M_\infty}^2 z^{2(1-2n)}} , \tag{34}$$

where the Mach number is based on axial velocity and sound speed at the edge of the region of interest. In the limit as $Re \rightarrow \infty$, the following set of ordinary differential equations (with primes denoting derivatives with respect to the scaled radial coordinate $\tilde{\phi}$) is obtained:

$$-\tilde{\phi}\left[\tilde{\rho}\left(n\tilde{w} - \frac{\tilde{u}}{\tilde{\phi}}\right)\right]' + \frac{2\tilde{\rho}\tilde{u}}{\tilde{\phi}} = 0 \tag{35a}$$

$$\frac{\gamma - 1}{\gamma}\left(\tilde{\rho}\tilde{T}\right)' - \frac{\tilde{\rho}\tilde{v}^2}{\tilde{\phi}} = 0 \tag{35b}$$

$$\tilde{\rho}\left(\tilde{u} - n\tilde{\phi}\tilde{w}\right)\tilde{v}' + \frac{\tilde{\rho}\tilde{u}\tilde{v}}{\tilde{\phi}} = \tilde{\mu}\left(\tilde{v}'' + \frac{\tilde{v}'}{\tilde{\phi}} - \frac{\tilde{v}}{\tilde{\phi}^2}\right) + \tilde{\mu}'\left(\tilde{v}' - \frac{\tilde{v}}{\tilde{\phi}} + n^2\tilde{\phi}^2\tilde{v}'\right) \tag{35c}$$

$$\tilde{\rho}\left(\tilde{u} - n\tilde{\phi}\tilde{w}\right)\tilde{w}' + \tilde{\rho}n\tilde{v}^2 = \tilde{\mu}\left(\tilde{w}'' + \frac{\tilde{w}'}{\tilde{\phi}}\right) + \tilde{\mu}'\tilde{w}' \tag{35d}$$

$$\tilde{\rho}\left(\tilde{u} - n\tilde{\phi}\tilde{w}\right)\left(\tilde{T}' - \frac{\tilde{v}^2}{\tilde{\phi}}\right) = \frac{1}{Pr}\left(\tilde{T}'' + \frac{\tilde{T}'}{\tilde{\phi}}\right) + \tilde{\mu}\left[(\tilde{w}')^2 + \left(\tilde{v}' - \frac{\tilde{v}}{\tilde{\phi}}\right)^2\right], \tag{35e}$$

where the Prandtl number in the energy equation is based on the reference viscosity and thus is a constant. These equations have the following boundary conditions:

$$\tilde{\phi} = 0 : \begin{cases} \tilde{u} = 0 \\ \tilde{v} = 0 \\ \tilde{w}' = 0 \\ \tilde{T}' = 0 \end{cases} , \qquad \tilde{\phi} = \tilde{\phi}_e : \begin{cases} \tilde{v}' = f(\Gamma) \\ \tilde{w} = 1 \\ \tilde{\rho} = 1 \\ \tilde{T} = \frac{1}{(\gamma-1){M_\infty}^2} \end{cases} . \tag{35f}$$

If the viscosity is assumed to have a power-law variation with temperature:

$$\mu = \left(\frac{T}{T_\infty}\right)^\sigma \tag{36}$$

(where T is the unscaled temperature,) then the only parameters in these equations are the Prandtl number Pr, the axial Mach number at the outer boundary M_∞, the viscosity-law exponent σ and the slope of the swirl velocity at the outer boundary, which sets the strength of the vortex (and is no longer a simple function of the circulation as it was in the incompressible case.)

As in the incompressible case, there is again an analytical solution of these equations for the special case of $n = 0$, representing a solid–body rotation with constant axial velocity, constant temperature and zero radial velocity. The density in this case is given by:

$$\tilde{\rho} = exp\left\{-\frac{\tilde{\phi}_{max}^2}{2}\left(\frac{\gamma}{\gamma - 1}\right) f^2 \left[1 - \frac{\tilde{\phi}^2}{\tilde{\phi}_{max}^2}\right]\right\} , \tag{37}$$

and is nonzero everywhere in contrast to the density for the inviscid case given by equation (25). Since there is no fluid entrainment in this columnar case, there can be no heat transfer in the steady solution, so the temperature is constant.

For the general case of nonzero growth rate the equations (35) have no nontrivial analytical solutions; they are rewritten as a set of eight first–order equations, discretized using central differences and solved numerically. Convergence to double–precision machine zero typically takes 10 to 15 iterations on a grid fine enough to guarantee a mesh–converged solution.

Results for $Pr = 0.72$ (air) and constant viscosity are presented in Figures 18-27, all for a maximum swirl velocity of 0.5. For reasons to be explained later, the conical ($n = 1$) model was chosen for the presented results, rather than the parabolic. However, as was found for the incompressible case, the difference between solutions at different $n > 0$ is quantitative rather than qualitative.

Figures 18, 19 and 20 show swirl, axial and radial velocity distributions for various Mach numbers up to nearly the limiting Mach number for $v_{max} = 0.5$. At low Mach number, the velocity plots look like those for the incompressible vortex. As the Mach number rises, the slope of the swirl velocity at the outer boundary changes sign, as was seen in the inviscid results of Section 2.3; the slope of the swirl velocity near the axis decreases. The axial velocity peak in the core region becomes less pronounced as the Mach number rises; near the limiting Mach number the axial velocity profile appears flattened out, the peak near the axis seen at low Mach numbers having completely disappeared. The radial velocity u is negative everywhere at very low Mach numbers, as it was in the incompressible case. As M_∞ rises, the radial velocity initially becomes positive in a small region near the axis and is positive everywhere near the limiting Mach number, indicating that the fluid in the core is expanding.

Figure 21 shows the static pressure coefficient. As was seen in the inviscid case, the static pressure coefficient profiles become flattened out at higher Mach numbers and the magnitude of the drop in C_p at the axis is reduced as the Mach number increases. It should be noted that this does not mean that the pressure in the core of the compressible vortex is actually higher than that in the incompressible case – the pressure coefficient is normalized with $\rho_e {w_e}^2$, which is also increasing as M_∞ increases. The distribution of C_p, however, is much less localized in the core at higher Mach numbers.

Figures 22 and 23 show distributions of density and temperature in the core. As in the inviscid case, the density reaches a minimum on the axis, but viscous effects prevent a vacuum region, although for some of the cases studied, the axis density was less than one one–thousandth of the free–stream density. The temperature decreases monotonically from the outer boundary to the axis, and the magnitude of the temperature drop is greater at higher Mach numbers. For the cases having $v_{max} = 0.5$, the axis temperature at $M_\infty = 4.5$ (close to the limiting Mach number of $2\sqrt{5}$) is less than 40 percent of the free–stream temperature. It was also found that the achievable temperature minimum depends on the Mach number – at low values of M_∞, the core temperature near the limiting velocity can be less than one tenth of the free–stream value, although the swirl velocities required to achieve this are high enough to make an experimental simulation of such a flow doubtful. At higher Mach numbers, however the swirl velocities required to produce a substantial temperature drop are quite reasonable.

An interesting result is the effect of compressibility on the vorticity distribution in the core, shown in figure 24. For the incompressible vortex there exists a concentrated core of high vorticity near the axis. It can be seen that as the Mach number increases, this vorticity peak becomes less pronounced and completely disappears at the limiting Mach number for the given swirl velocity. This means that for the compressible vortex, the core (as defined by its increased vorticity) may be ill-defined or disappear altogether. For this reason, the rate-of-growth arguments which were used for the incompressible vortex do not hold here – the compressible core at higher Mach numbers seems to expand and fill all the space available to it. In the case of compressible flow over a delta wing at incidence, the core will fill the region inside the shear layer rolling up from the leading edge and thus grow in a roughly conical fashion. This is the reason why a linear growth rate ($n = 1$) was chosen for the presented results.

Figures 25 and 26 show distributions of axial and total Mach number, normalized with M_∞, all for $v_{max} = 0.5$. The plots of axial mach number look much like the plots of axial velocity; one difference is that while the peak value of axial velocity decreases as M_∞ becomes larger, the peak axial mach number ratio increases. It is evident that the total Mach number has a maximum away from the axis, indicating that the compressibility of the flow is greatest there.

The effects of varying the Prandtl number and the viscosity law were also investigated. Axis temperatures for $M_\infty = 1$, with $\tilde{v}_{max}$ as the independent coordinate, are presented in figures 27 and 28. It should be noted that each point on the curves shown represents an individual solution of equations (35) at some value of $\tilde{v}_{max}$, Pr and σ. It is evident that at a given maximum swirl velocity, the core temperature decreases as the Prandtl number is increased. This is because an increase in Prandtl number implies either a higher viscosity, which enhances the energy separation, or a lower thermal conductivity, which means less heat transfer into the core. Either leads to a lower temperature. It can also be seen in the figures that the core temperature first drops as the swirl velocity increases from zero, reaches a minimum, then begins to rise again. For a viscosity which is constant ($\sigma = 0$) or varies slowly with temperature, this temperature rise occurs for swirl velocities greater than the limiting swirl velocity ($\tilde{v}_{lim} = \sqrt{5}$,) meaning that for physically realizable flow conditions the temperature drops monotonically as the swirl velocity increases. For the viscosity law having $\sigma \geq \frac{1}{4}$, however, the temperature rises slightly before the limiting velocity is reached. The reason for this behavior is not clear at present. It was also found that as the viscosity–law exponent σ increases, the core

velocities are higher and the axis density decreases more rapidly with $\tilde{v}_{max}$, since the core viscosity is dropping as the temperature drops. The solutions show that the energy-separation effect effect can be quite pronounced – for free-stream axial Mach numbers of order one, the static temperature on the axis can reach values less then one–third the free-stream temperature for swirl angles on the order of 45 degrees.

3 Conclusions

Results have been presented for a new class of self–similar solutions of the Navier–Stokes equations modelling the flow in slender vortices. The approach is general, allows for treatment of both the viscous and inviscid limits at high Reynolds number, and the resulting equations can be readily solved numerically or even analytically in some special cases. For the incompressible case, results agree well with the experimental data of Earnshaw [1], showing high axial velocities and substantial pressure gradients in the core of the vortex. The present approach is compared to the conical vortex model of Powell and Murman [5] and the matched inner and outer solutions of Hall [3] and Stewartson and Hall [4]. In the absence of axial pressure gradients the viscous core of an incompressible vortex is shown to grow with the one–half power of the axial coordinate. The level of total pressure loss in the core appears to be dependent only on the maximum swirl velocity in the vortex.

New results are presented for compressible vortex cores. The inviscid rotational equations for a conical vortex are solved numerically and the results compared to those of Brown [6]. The results show that for the inviscid rotational vortex, the core swirl velocity goes to zero only when the density on the axis vanishes. The results of Brown at higher Mach numbers are shown to be nonphysical using limiting velocity concepts. The solutions of viscous equations for the compressible vortex show a decrease in axial velocity and suction peaks as the Mach number increases and low core temperatures near the limiting conditions. Compressibility appears to have a distributive effect on the vorticity in the core. Effects of variable viscosity and different Prandtl numbers are also studied.

Ongoing research includes a generalization of the present approach to study the rate of growth and other properties of vortex cores when an axial pressure gradient is present, somewhat analogous to the Falkner–Skan similarity solutions of laminar boundary–layer theory. Other topics of interest for future research are the stability properties of these self–similar viscous vortex cores and the effects of compressibility and axial pressure gradients on stability. Finally, the present solutions might serve as a useful basis for a study of vortex breakdown, since most studies of the subject to date appear to have suffered from a lack of physically realistic upstream conditions. The use of upstream conditions which are exact solutions of the Navier–Stokes equations would prevent the introduction of the artificial axial pressure gradients that overly simplistic model profiles introduce and at least provide a starting point for an accurate numerical investigation of the subject.

Acknowledgements

The authors would like to thank Earll Murman for helpful discussions during the development of the models for incompressible and compressible conical flow. This work was funded by the National Science Foundation (Grant EET–8857500) and by a Research Partnership Award from the Horace H. Rackham School of Graduate Studies, the University of Michigan.

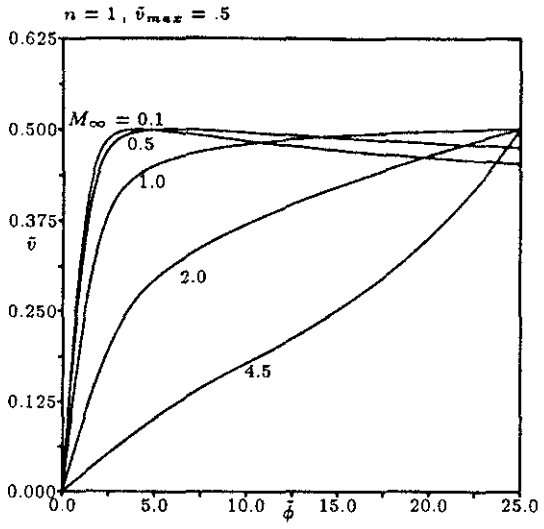

Figure 18: Compressible vortex – Swirl Velocity Distribution

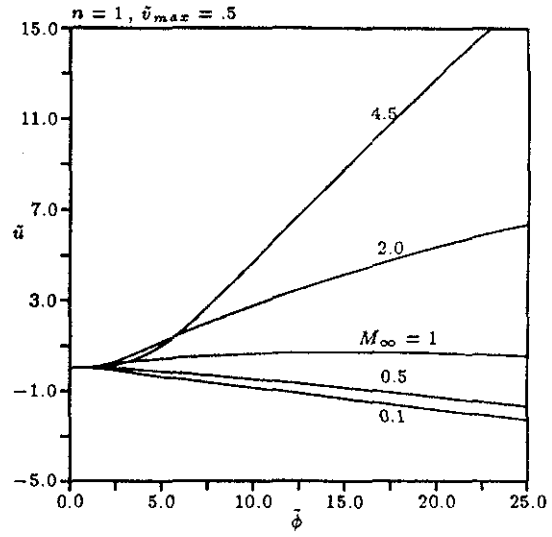

Figure 20: Compressible vortex – Radial Velocity Distribution

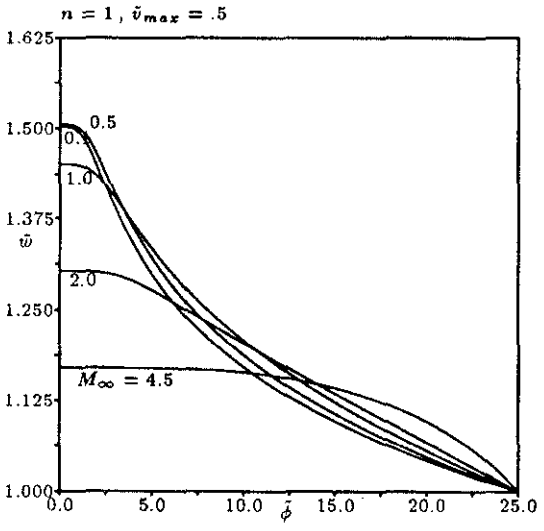

Figure 19: Compressible vortex – Axial Velocity Distribution

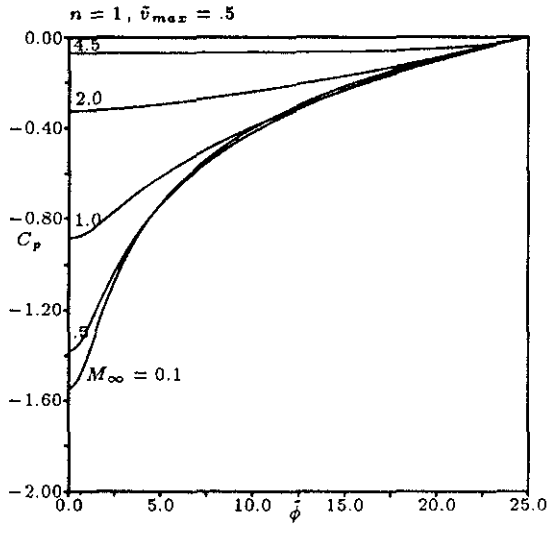

Figure 21: Compressible vortex – Static Pressure Distributions

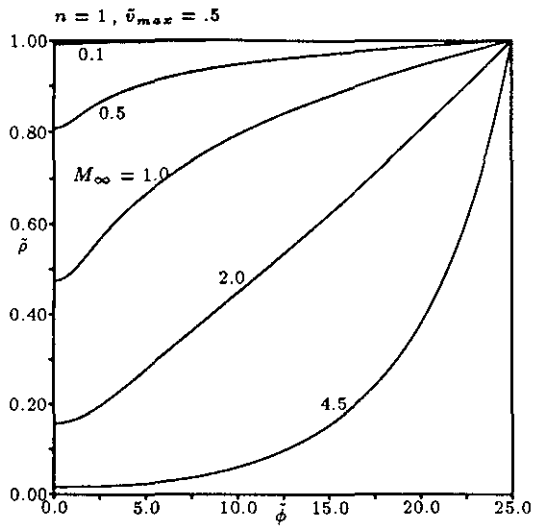

Figure 22: Compressible vortex – Density Distribution

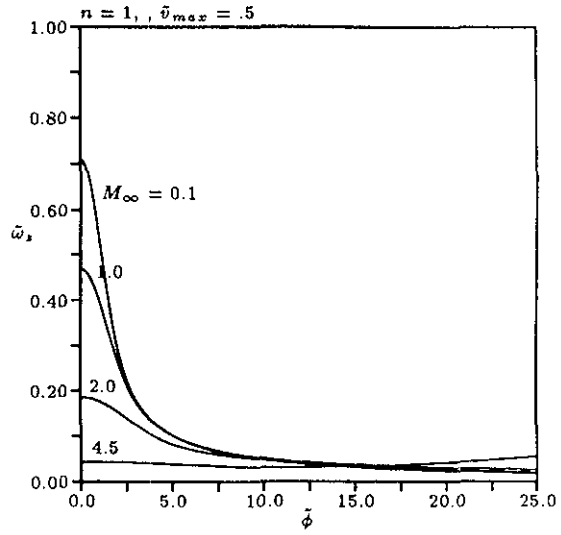

Figure 24: Compressible vortex – Vorticity Distribution

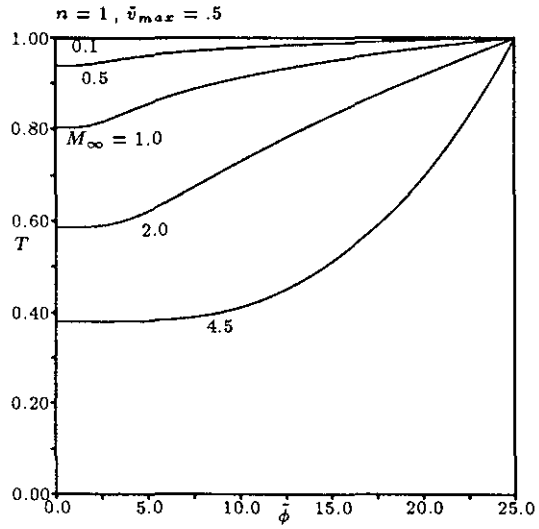

Figure 23: Compressible vortex – Temperature Distribution

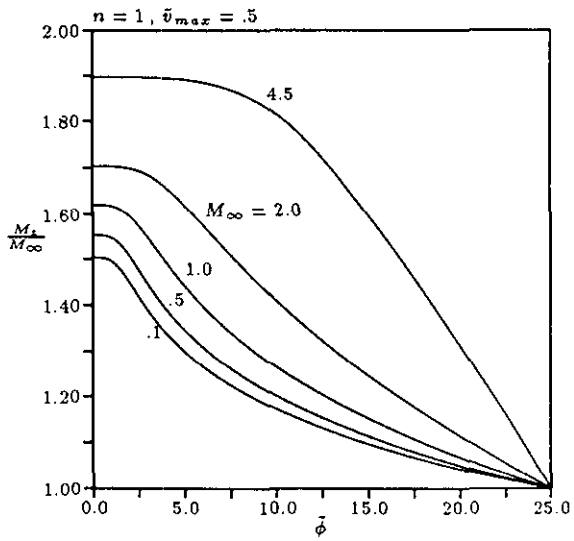

Figure 25: Compressible vortex – Axial Mach Number Distribution

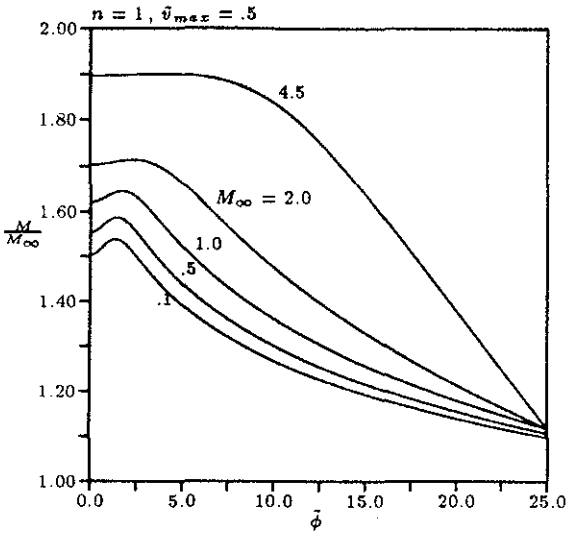

Figure 26: Compressible vortex – Total Mach Number Distribution

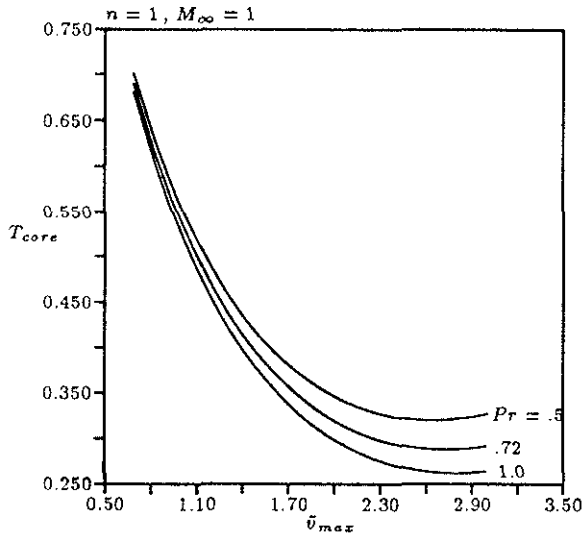

Figure 27: Compressible vortex – Axis Temperatures for various Prandtl numbers ($\sigma = 0$)

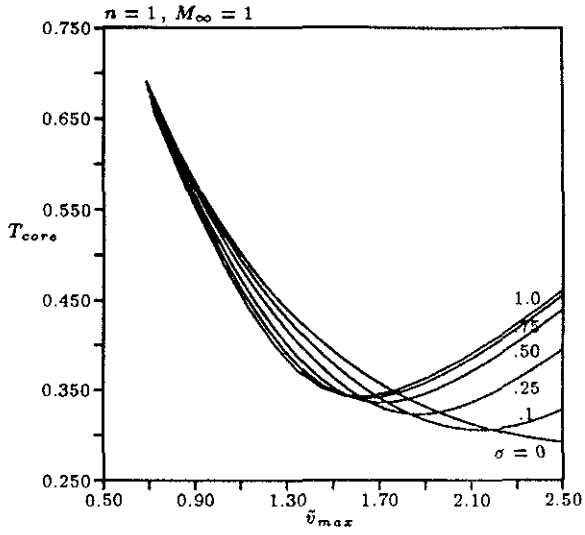

Figure 28: Compressible vortex – Axis Temperatures for various viscosity laws ($Pr = 0.72$)

References

[1] P. B. Earnshaw, "An experimental investigation of the structure of a leading-edge vortex," Reports and Memoranda 3281, Aeronautical Research Council, 1961.

[2] B. Monnerie and H. Werlé, "Étude de l'Écoulement supersonique et hypersonique autour d'une aile Élancée en incidence," in *AGARD-CP-30*, 1968.

[3] M. G. Hall, "A theory for the core of a leading-edge vortex," *Journal of Fluid Mechanics*, vol. 11, 1961.

[4] K. Stewartson and M. G. Hall, "The inner viscous solution for the core of a leading-edge vortex," *Journal of Fluid Mechanics*, vol. 15, 1963.

[5] K. G. Powell and E. M. Murman, "A model for the core of a slender viscous vortex," AIAA Paper 88-0503, 1988.

[6] S. N. Brown, "The compressible inviscid leading-edge vortex," *Journal of Fluid Mechanics*, vol. 22, 1965.

[7] L. M. Mack, "The compressible viscous heat-conducting vortex," *Journal of Fluid Mechanics*, vol. 8, 1960.

[8] M. G. Hall, "The structure of concentrated vortex cores," *Progress in the Aeronautical Sciences*, vol. 7, 1966.

[9] K. G. Powell, *Vortical Solutions of the Conical Euler Equations*. Vieweg, 1989. In press.

[10] P. M. Hartwich and C. H. Hsu, "An implicit flux-difference splitting scheme for three-dimensional, incompressible Navier-Stokes solutions to leading-edge vortex flows," in *AIAA 4th Applied Aerodynamics Conference*, 1986.

[11] P. M. Hartwich, C. H. Hsu, J. M. Luckring, and C. H. Liu, "Numerical study of the vortex burst phenomenon for delta wings," AIAA Paper 88-0505, 1988.

[12] E. M. Murman and K. G. Powell, "Comparison of measured and computed pitot pressures in a leading-edge vortex from a delta wing," in *Studies of Vortex-Dominated Flows*, pp. 270–281, Springer-Verlag, 1985.

[13] J. L. Thomas and R. W. Newsome, "Navier-Stokes computations of lee-side flows over delta wings," AIAA Paper 86-1049, 1986.